Holocene Earthquakes on the Tambomachay Fault near Cusco, Central Andes

Lorena Rosell [*,1], Carlos Benavente [1,2], Swann Zerathe [1,3], Sam Wimpenny [4], Enoch Aguirre [1], Richard Walker [5], Christoph Grützner [6], Briant García [1], Laurence Audin [3], Andy Combey [3], Anderson Palomino [1], Fabrizio Delgado [2], Miguel Rodríguez-Pascua [7], José Cardenas [8], Julien Carcaillet [3]

[1] Instituto Geológico, Minero y Metalúrgico (INGEMMET), San Borja, Perú | [2] Especialidad Ingeniería Geológica, Facultad de Ciencias e Ingeniería. Pontificia Universidad Católica del Perú | [3] Univ. Grenoble Alpes, Univ. Savoie Mont Blanc, CNRS, IRD, IFSTTAR, ISTerre, 38000 Grenoble, France | [4] COMET, School of Earth and Environment, University of Leeds, Leeds, UK | [5] COMET, Dept. of Earth Sciences, Oxford University, South Parks Road, Oxford OX1 3AN, UK | [6] Friedrich Schiller University Jena, Institute of Geological Sciences, Burgweg, 11 07749 Jena, Germany | [7] Instituto Geológico y Minero de España (IGME, CSIC). Ríos Rosas Street 23, 28022-Madrid, Spain | [6] Universidad Nacional de San Antonio Abad del Cusco (UNSAAC), Peru

Abstract   The city of Cusco (Peru, Central Andes) has been severely damaged by several major earthquakes during pre-Hispanic times, and more recently in 1650 and 1950 CE. While the sources of those earthquakes are unknown, a system of active normal faults trending SE-NW and cutting Quaternary glacial deposits borders the city to the north. A detailed neotectonic study of these faults is therefore needed to build an understanding of the seismic hazard in the region. We focus on the fault segment that is closest to the city, the Tambomachay Fault, a 20-km-long normal fault running along the northern margin of the Cusco Basin, and present new geomorphological and paleoseismic evidence for multiple Holocene earthquakes along this structure. The western segment of the fault preserves fault scarps that cut moraine crests with a mean fault throw of 4.0 ± 0.3 m. We determined a 14.2 ± 0.5 kyr depositional age of these moraines using 10Be cosmogenic surface-exposure dating of boulders embedded in the moraines, implying a Holocene-average fault slip rate range from 0.30 to 0.37 mm/yr. We also excavated a trench across the moraine crests. By reconstructing the trench stratigraphy with radiocarbon dating, we identified three surface-rupturing earthquakes over the last 8–9 kyr. The oldest earthquake occurred between 8.5 and 8.3 kyr, a second event between 6.8 and 5.5 kyr, and the most recent earthquake between 1.2 and 0.9 kyr. All of the ruptures predate Inca times (>1 kyr), thus historical earthquakes that affected the city of Cusco were not produced along this fault segment and may have originated from the rupture of other structures nearby. Nevertheless, surface-rupturing earthquakes along the Tambomachay Fault are likely to have had moment magnitudes of M_w 6.4–6.9. Similar future events may have the capacity to severely damage modern-day Cusco due to their proximity to the city, which now has a population of 500 000.

1 Introduction

Subduction of the Nazca Plate under the western margin of South America has led to the uplift of the Andes mountains, and makes Peru one of the most seismically active regions in the world with large magnitude (M_w > 8) megathrust earthquakes every few decades causing destruction in urban areas along the coast (*Molnar*, 1979; *Villegas-Lanza et al.*, 2016). However, within the overriding plate there are many active faults that have an uncertain seismogenic potential (*Audin et al.*, 2007; *Macharé Ordoñez et al.*, 2009; *Benavente et al.*, 2013, 2017; *Wimpenny et al.*, 2020; *Aguirre et al.*, 2021). In particular, the Altiplano of southern Peru is slowly extending along a system of E-W- to NW-SE-striking normal faults, and the low deformation rates imply that individual faults

have recurrence times of many thousands of years. Therefore, catalogues of earthquakes are a poor indicator of the rate and distribution of seismicity (*Machette*, 2000). The historical record of earthquake shaking indicates that a number of these faults are able to produce moderate-magnitude earthquakes that would pose a significant hazard to urban centres (*Silgado*, 1978), though quantitative estimates of the timing and magnitudes of historical earthquake are still sparse. Identifying geomorphological evidence for past earthquakes from fault scarps, and estimating their timing and magnitude using paleoseismology, can address this issue by extending the earthquake catalogue back in time.

Cusco is situated along the northern margin of the Peruvian Altiplano and has a long history of destructive earthquakes that have caused heavy
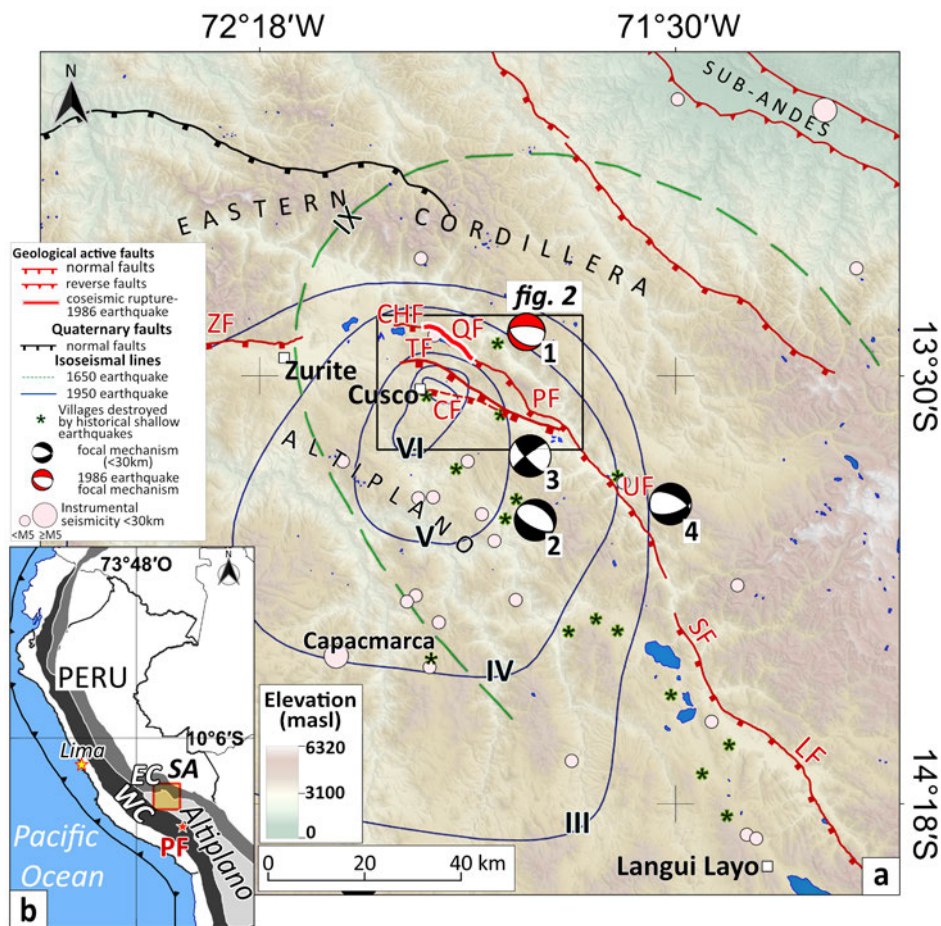
Figure 1 – a) Overview map of mapped active faults (red lines) in the Altiplano-Eastern Cordillera region of south Peru. Red lines with white borders represent the proposed surface rupture of the 1986 earthquake. The black lines represent Quaternary normal faults. Blue lines are the isoseismal lines of the 1950 earthquake (denoted by Roman numerals) (*Ericksen et al.*, 1954; *Silgado*, 1978), and green dashed lines are the isoseismal lines of the 1650 earthquake (*Tavera et al.*, 2016). All focal mechanisms are taken from the GCMT catalogue of *Ekström et al.* (2012): 1 is the focal mechanism of the 1986 earthquake, 2 is the focal mechanism of a 2003 earthquake, 3 is the focal mechanism of a 2014 earthquake and 4 is the focal mechanism of a 2015 earthquake. The instrumentally recorded seismicity is shown in pink circles (*Datos Sísmicos*, 2022). From north to south the abbreviations are: ZF-Zurite Fault, CHF-Chinchero Fault, TF-Tambomachay Fault, QF-Qoricocha Fault, CF-Cusco Fault, PF-Pachatusan Fault, UF-Urcos Fault, SF-Sangarara Fault and LF-Langui Fault. **b)** Inset map of the location of the study area (a) denoted by the yellow rectangle with red border and in respect to the main morphological units of the Andes (WC, Western Cordillera; Altiplano; EC, Eastern Cordillera; SA, Sub-Andean zone), and the city of Lima (yellow star). The Parina Fault (PF) is shown by the red star with a white border.

damage to the city, particularly three events in 1650, 1950 and 1986 (*Ericksen et al.*, 1954; *Silgado*, 1978; *Cabrera and Sébrier*, 1998) (Figure 1). The city is located within a 15-km-long, 3-km-wide hanging-wall basin of the ~E-W striking Cusco, Qoricocha, Tambomachay, Chinchero, and Pachatusan normal faults (*Sébrier et al.*, 1985; *Cabrera Nuñez*, 1988; *Mercier et al.*, 1992; *Benavente et al.*, 2013) (Figure 2a and 2b). These faults have been mapped on the basis of their geomorphological expression and the distribution of fault scarps that cut through recent glacial deposits that form the cover sediment around Cusco (*Sébrier et al.*, 1985; *Cabrera Nuñez*, 1988; *Mercier et al.*, 1992; *Benavente et al.*, 2013; *Wimpenny et al.*, 2020). By far the most prominent of these faults is the Tambomachay Fault, which outcrops 2–3 km north of the city and is delineated by 300-m-high, south-dipping triangular facets that extend for 20 km between the Sencca Hills and

Larapa (*Sébrier et al.*, 1985; *Cabrera Nuñez*, 1988; *Mercier et al.*, 1992; *Benavente et al.*, 2013; *Wimpenny et al.*, 2020) (Figure 2a). A number of fault scarps offset glacial moraines near the base of these triangular facets at Sencca Hills, suggesting that part of the Tambomachay Fault has been active since the last glacial retreat. However, the ages of the moraines are still unknown and previous efforts to study the slip rate on the Tambomachay Fault have been based on the assumption that the moraines are of Late Glacial Maximum age (~10–45 kyr; e.g., *Wimpenny et al.*, 2020).

In this study, we combine historical accounts of earthquakes in Cusco with aerial imagery, high-resolution Digital Elevation Models (DEMs), paleoseismic trenching, radiocarbon dating, and cosmogenic exposure dating to reconstruct the Holocene history and magnitude of surface-rupturing earthquakes on the Tambomachay Fault. We
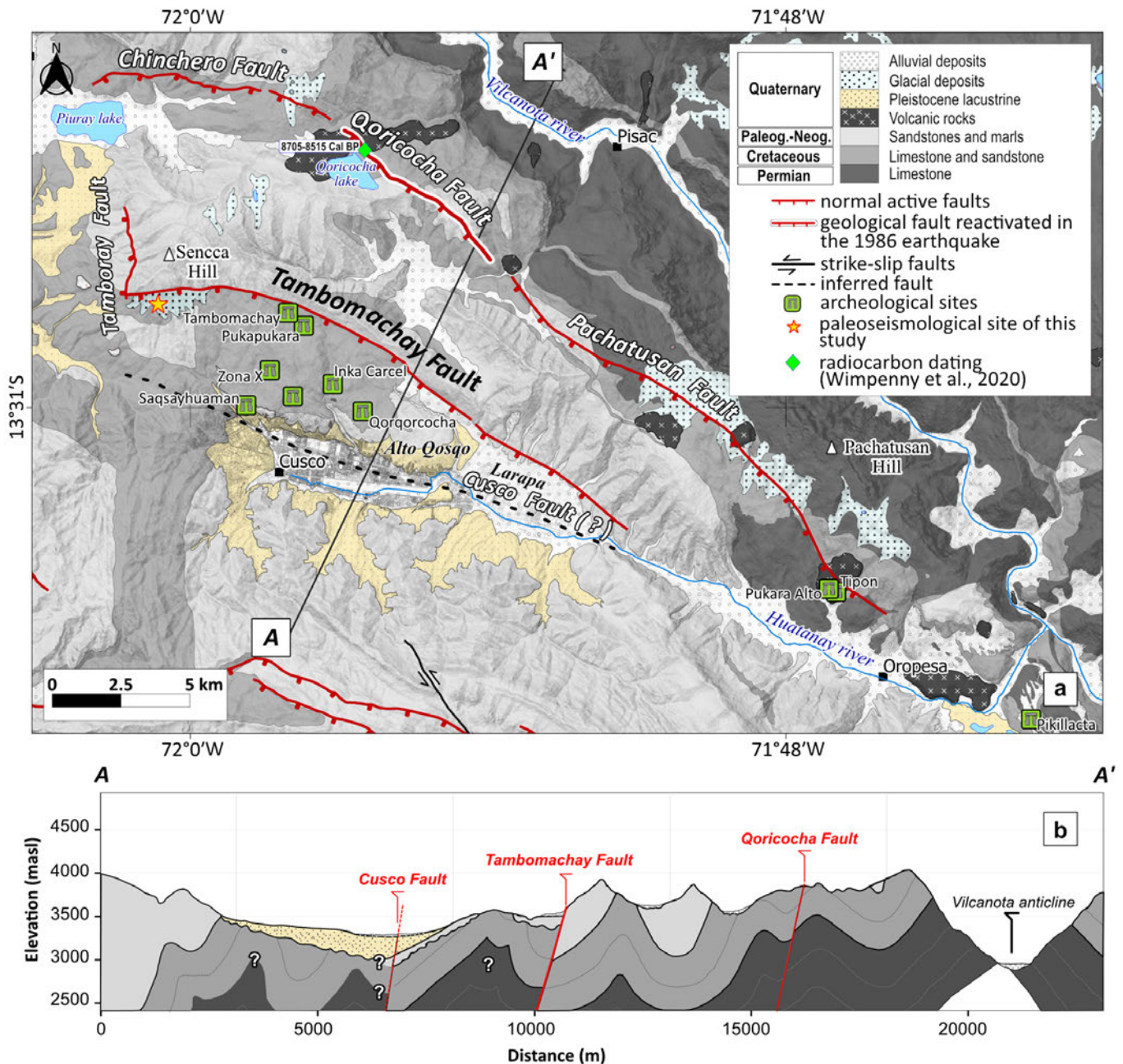
Figure 2 – a) Geological map of the Cusco Basin (modified from *Carlotto et al.*, 2010). The dark gray color represents Permian (Paleozoic) limestone, the grey color represents Cretaceous rocks, the light grey color represents Paleogene-Neogene sandstones and marls, and the mottled yellow color represents Pleistocene lacustrine deposits. Mottled light blue colors represent Late-Quaternary glacial deposits, and the mottled white color represents Late-Quaternary alluvial deposits. The red lines represent active faults (*Benavente et al.*, 2013). The green symbols represent major archeological sites. The paleoseismic site of this study is indicated by the yellow star. **b)** Structural section A-A', which shows the Tambomachay Fault, which juxtaposes Cretaceous rocks and Late-Quaternary alluvial deposits with Paleogene-Neogene rocks.

focus on this fault in particular because of its well-preserved scarps, its clear geomorphological expression, and its proximity to the city of Cusco. Our new observations are critical to understanding the seismic hazard to the city, which has rapidly expanded from a population of 60 000 in 1950 to around 500 000 by 2020.

2 Tectonic Setting

The Tambomachay Fault sits along the northern margin of the Altiplano-Puna plateau, a ~1800-km-long and 250–300-km-wide low-relief plateau that extends from southern Peru to northern Argentina. Uplift of the Altiplano-Puna plateau took place in response to a compressional tectonic regime associated with the subduction of the oceanic Nazca Plate under the continental South American Plate. The principal phase of uplift is considered to be late Miocene in age (e.g., *Oncken et al.*, 2006; *McQuarrie et al.*, 2008), but today the active faulting in the Peruvian Altiplano is predominantly extensional (*Sébrier et al.*, 1985; *Benavente et al.*, 2013; *Wimpenny et al.*, 2020; *Aguirre et al.*, 2021). A

system of E-W- to NW-SE-trending active normal faults has been mapped from the northern extremity of the Peruvian Altiplano to its southwestern edge in the Western Cordillera (*Sébrier et al.*, 1985; *Mercier et al.*, 1992) (Figure 1). Measurements of the kinematics of these faults show they have accommodated ~N-S to ~NE-SW extension since at least the Middle Pleistocene (*Sébrier et al.*, 1985; *Mercier et al.*, 1992; *Wimpenny et al.*, 2020). Those normal faults have reactivated (inverted) an old fault system inherited from Paleogene to Neogene to compressive phases (Figure 2a and 2b). The Cusco Basin is the northern-most expression of this extensional faulting in the Altiplano and consists of an E-W-trending Late-Quaternary intra-montane basin filled with lacustrine and alluvial sediments within the hanging-walls of the Cusco, Tambomachay, Chincheros, Qoricocha, and Pachatusan normal faults (*Sébrier et al.*, 1985; *Cabrera Nuñez*, 1988; *Mercier et al.*, 1992; *Benavente et al.*, 2013) (Figures 1 and 2). The Cusco Fault is inferred to run along the northern margin of the basin where a sharp change in stream incision occurs between Alto Qosqo and the Cusco Basin, though there is no direct evidence for this fault in the form of fault scarps or offset stratigraphy (Figure 2).The Tambomachay Fault has a much more evident imprint though the landscapes, as marked by 300-m-high, south-dipping triangular facets that extend for 20 km between Sencca Hills and Larapa and by outcrop with fault trace and offset visible along 2 to 3 kilometers north of the Cusco Basin (*Sébrier et al.*, 1985) (Figures 2a and 3a). The fault juxtaposes Cretaceous rocks in the hanging-wall with Paleogene-Neogene rocks in the footwall (*Carlotto*, 1998) (Figure 2). The western section of the fault reaches the surface at ~4000 m elevation in the mountains north of the Cusco Basin, while the eastern section of the fault outcrops along the basin margin near Larapa (Figure 2). Around ten kilometers north of Cusco, a series of discontinuous fault scarps 3 to 20 m high are visible, cutting glacial deposits in the mountains. These are the Chinchero, Qoricocha, and Pachatusan Faults. Recent sedimentation around the Cusco Basin has been dominated by glaciation, which has left behind extensive drift sheets and moraines (Cabrera, 1988). Although no absolute dating of the glacial deposits around Cusco has been undertaken, radiocarbon dating of peat underlying moraines in the nearby Eastern Vilcabamba (Figure 1) suggests a major period of glacial deposition around ~10–45 kyr (*Clapperton*, 1983). One radiocarbon date from a colluvial wedge overlying the glacial drift on the Qoricocha Fault suggests the drift deposits are at least 8 kyr old (*Wimpenny et al.*, 2020), indicating the fault scarps around Cusco are probably Holocene in age.

Records of instrumental and historical seismicity around Cusco provide additional constraints on the size and timing of past fault slip events (*Silgado*, 1978). The instrumental record in the study area is limited to

the last 60 years. Recorded shallow earthquakes (<30 km) have magnitudes less than M_w 5.4 (Figure 2). The only instrumentally recorded moderate-magnitude earthquake occurred on April 5th 1986, when Cusco city was hit by a M_w 5.4 shallow normal-faulting earthquake (red focal mechanism in Figure 1) that resulted in 7 fatalities, 80 wounded, and more than 13,000 people affected (*Huamán*, 1987; *Silgado*, 1978). Shaking recorded withing the Cusco Basin was VII on the modified Mercalli scale (*Cabrera and Sébrier*, 1998). *Cabrera and Sébrier* (1998) identified by 10-cm-high surface ruptures for ~3 km along the foot of 4–6 m-high Holocene fault scarps north of Qoricocha Lake, and suggesting that the 1986 earthquake was generated by slip on the Qoricocha Fault (Figures 1 and 2). Paleoseismic trenching across the fault revealed offset colluvial wedges overlying Holocene glacial drift, indicating at least 3 surface-rupturing earthquakes on the Qoricocha fault since the moraines were deposited at >8 kyr (*Cabrera and Sébrier*, 1998; *Wimpenny et al.*, 2020). The focal mechanisms of a few other earthquakes in the instrumental record (Figure 1) indicate dip-slip and strike-slip movements.

The historical seismicity sources cover significant events since the time of the Incas (*Silgado*, 1978; *Gisbert*, 1999). The earthquake of May 21st 1950 was the most recent historical event with a probable magnitude of M_w 6. This earthquake hit Cusco and caused severe damage to the city (*Silgado*, 1978). The U.S. Coast and Geodetic Survey estimated a provisional position of the earthquake epicenter to be 50 km south of the city of Cusco near the town of Capacmarca (*Ericksen et al.*, 1954). *Ericksen et al.* (1954) estimated a peak intensity of VII (modified Mercalli scale) in the Cusco Basin from field observations, interviews, letters, and building damage. This suggests that the earthquake was of tectonic origin and due to the reactivation of a fault close to the city (*Ericksen et al.*, 1954).

Another important major earthquake in the historical catalogue of (*Silgado*, 1978) occurred on March 31st 1650. Written accounts associated with the earthquake are limited, and mainly derived from Spanish colonial documents and correspondence. A Christian priest in Cusco reported that *"all of the temples and buildings were destroyed"* and that *"in the town of Yaurisque [10 km south of Cusco] everything was destroyed"* (*Palma*, 1901; *Silgado*, 1978). *Silgado* (1978) reports that damage occurred in towns that are 100-150 km west of the city of Cusco and that the earthquake was felt in Lima. The wide reports of damage from this earthquake suggest that it might have been far larger than the 1950 and 1986 earthquakes. Also, the intensity in the epicentral area was estimated to be IX on the modified Mercalli scale by *Tavera et al.* (2016) (Figure 1). The earthquake probably had a magnitude of M7.2 (*Silgado*, 1978). As the most severe damage was located in Cusco, this event is not thought to have occurred within the subducting Nazca Plate.

One account of pre-1650 seismicity is reported by *Gisbert* (1999) mentions that in the period of Inca Pachacutec (AD 1418–1471) *"the city of Cusco trembled for several minutes, remaining dark for hours; people mentioned that they saw an eagle come out of hills northeast of the city of Cusco. In it had an Amaru (snake in Inca language), which had been torn from the interior of the earth, at that moment they saw a long continuous line of ~3 leagues [~15 km] that was formed on the landscape between the Pachatusan and Sencca hills"* (Figure 2). These eye-witness reports are consistent with an earthquake rupturing the surface on a fault in the hills north of Cusco, where the Tambomachay, Qoricocha and Pachatusan Faults crop out.

3   Morphology of the Tambomachay Fault Scarps

3.1   Method of Fault Scarp Mapping

We mapped the scarps of the Tambomachay Fault using three independent data sets. For the western section of the fault, we used Pléiades 0.5 m panchromatic and 0.7 m multispectral images acquired on 15th February 2019, plus a high-resolution DEM formed from the panchromatic stereo-image pair of the same images built with the photogrammetry software Ames Stereo Pipeline (*Broxton and Edwards*, 2008) following the procedure of *Beyer et al.* (2018). The resulting DEM has a point cloud density of 1.53 m/px and covers the region between Sencca Hill and Larapa. We also formed a 0.2 m/px DEM over the Sencca Hill area from aerial photographs collected using an eBee senseFly drone and the structure-from-motion technique implemented in Agisoft PhotoScan (*Agisoft*, 2018).

On the eastern section of the fault, recent construction and earthworks shroud geomorphological evidence of the fault trace. Therefore, to map evidence of fault scarps north and east of Larapa, we used historical aerial photographs taken in 1956 held by the Peruvian Ministry of Culture. We generated a DEM from the aerial photographs using the structure-from-motion method with Agisoft PhotoScan (*Agisoft*, 2018; *Westoby et al.*, 2012). Where features could be identified in both the historical and modern imagery, we used them as ground control points to guide the image matching and georeferencing of the photographs. The resulting DEM and orthomosaic have a resolution of 1.26 m/px.

The DEMs allow us to not only map the locations of the fault scarps, but also to measure their offsets and associated uncertainties and to deduce the fault throw (fault vertical offset). For this, we followed the workflow detailed in *Benavente et al.* (2021) and *Benavente et al.* (2022) that was based on the methodology proposed by *Mackenzie and Elliott* (2017). It consists of three steps: (1) we estimated the scarp offset using the established method of extracting profiles perpendicular to the fault scarp in areas where the surfaces in the hanging-wall can be correlated with the surfaces in the footwall (e.g. moraines crests and flanks, linear and homogenous slopes). We fit lines to these surfaces and calculated the scarp offset between them at the foot of the scarp (see Figure SI-1 for topographic profile locations and Figure SI-2 for each individual topographic profile, in the Supporting Information). (2) We converted the fault offset into a fault throw (see Table SI-1, in the Supporting Information) according to local measurements of the fault dip. Here we used fault dip ranging from 50 to 70°corresponding to the mean of several measurements performed around the paleoseismic trench. (3) We analysed the statistical distribution of the fault throws to deduce a weighted mean and its associated uncertainty along the fault segment. Finally, a range of most probable mean slip fault values was calculated using the fault dip ranging from 50 to 70°and considering that the fault shows an almost purely normal slip component (rake = ~90°).

3.2   Fault Scarp Observations

The Tambomachay Fault scarps can be mapped between the Sencca Hills and the Larapa sector using the optical satellite imagery and high-resolution DEMs (Figure 3a). We divide the fault into three different sections along its trace: the Sencca sector, the Pumamarca sector, and the Larapa sector (Figure 3a).

The Sencca sector corresponds to the western tip of the Tambomachay Fault and consists of three strands of well-preserved, south-facing fault scarps cutting lateral moraines just south of the bedrock-moraine contact (Figures 2a, 3a and 3c). The scarps have a mean strike of 98°, the dip ranges between 50 and 70°, and they can be traced for 3 km along strike. The scarp offset in this sector varies between 2.2 ± 0.6 m to 8.4 ± 0.3 m, and the equivalent fault throw varies between 2.8 ± 0.6 m and 9.0 ± 0.7 m (Figure 3b and Table S1). The highest value of fault throw (9.0 ± 0.7 m) was measured in the valleys between the moraine crests and may correspond to an outlier affected by erosion. Excluding this value, the fault throws in the Sencca sector are tightly grouped between 2.8 and 5.0 m, with a weighed-mean of 4.0 ± 0.3 m (error of the weighed-mean) and a standard deviation of 0.9 m (Figure 3b). The fault throw value obtained along the moraine crest (4.1 ± 0.8 m; Figure 3c), where the paleoseismic trench is located, is very close to this weighted mean.

The Pumamarca sector is ~12 km long and corresponds to the central part of the Tambomachay Fault (Figure 3a). In this region, the fault footwall is incised by narrow, south-draining streams, and the stream incision terminates abruptly across the inferred fault trace. We extracted ten topographic profiles perpendicular to the fault scarps from the high-resolution DEMs in this area. Two of the topographic profiles were measured on displaced
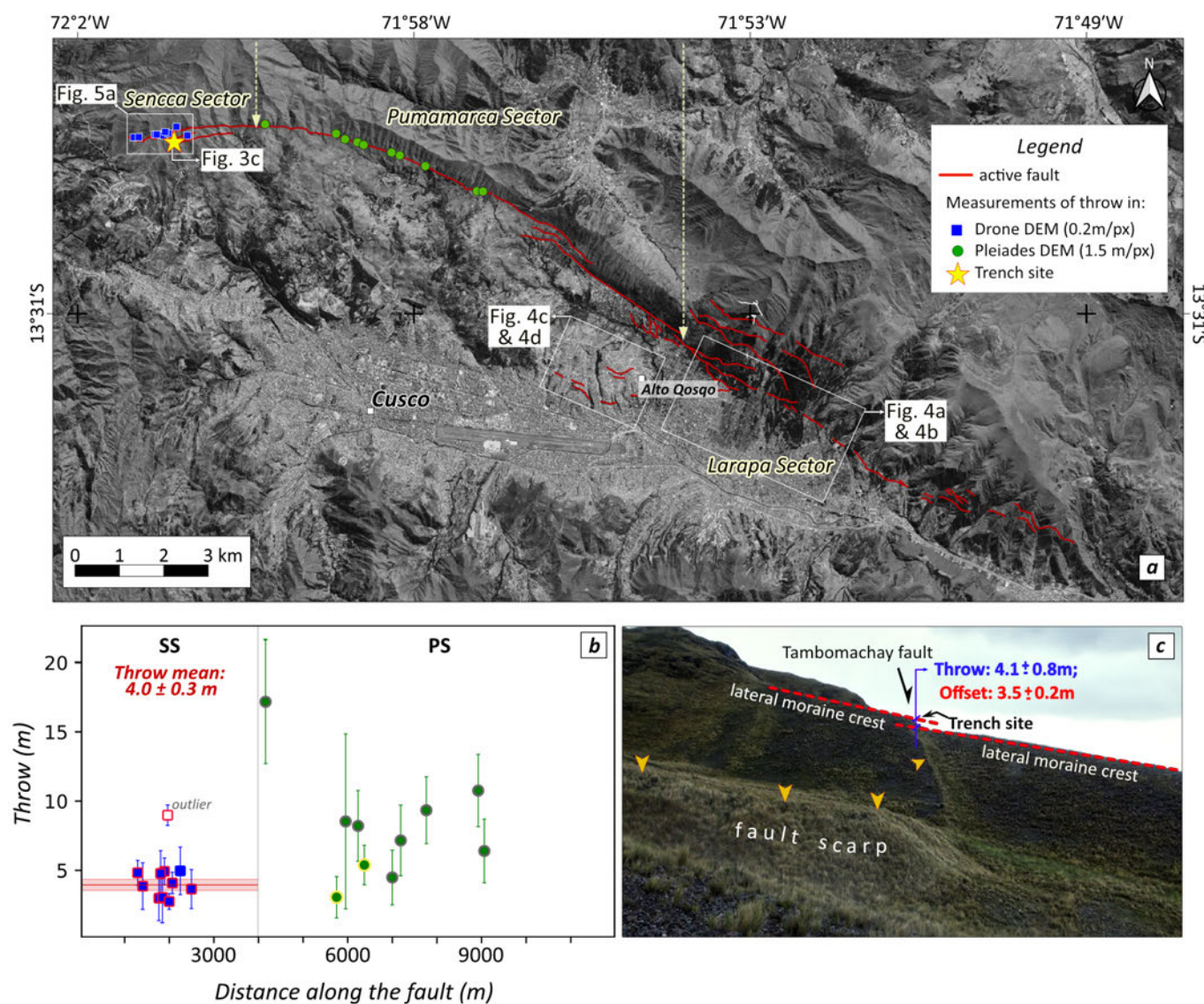
Figure 3 – **a)** Optical satellite imagery (from Google, DigitalGlobe) of the detailed mapping of Tambomachay Fault scarps along the sectors: Sencca (SS), Pumamarca (PS) and Larapa. The yellow dashed lines delimit the sectors along the fault trace. The blue squares indicate the location of scarp offset measurements from the 11 fault-perpendicular profiles extracted from the high-resolution DEM (0.2 m/px). The green circles indicate the location of scarp offset measurements from the 10 fault-perpendicular profiles extracted from the high-resolution DEM (1.5 m/px). The yellow star indicates the location of the paleoseismic trench. **b)** Scatter plot of the variability of throw measurements with their respective uncertainties along the Tambomachay Fault. The blue squares with red borders represent measurements on Holocene fluvio-glacial deposits, while the borderless blue square represents a measurement on bedrock. The red line represents the mean throw value in the Sencca Sector and its buffer represents the error of the weighted-mean. The green circles with yellow borders represent measurements on Quaternary alluvial deposits, while green circles with grey borders represent measurements on bedrock. **c)** Field photograph with profile view of a lateral moraine in the Sencca Sector. The yellow triangles indicate the Tambomachay Fault scarp. The throw measurement value, and location of the paleoseismic trench on the displaced lateral moraine crest are also indicated.

alluvial surfaces with vertical offsets between 2.5 ± 0.6 m and 4.5 ± 0.6 m, which are equivalent to fault throw values of 3.1 ± 1.5 m and 5.4 ± 1.4 m, respectively (Figure 3b and Table SI-1, in the Supporting Information). The other eight profiles were measured across bedrock scarps and recorded vertical offsets between 3.3 ± 0.5 m and 13.4 ± 1.3 m, with equivalent fault throw values between 4.5 ± 2.0 m and 17.2 ± 5.5 m (Figure 3b).

The variability of fault throw values along the fault trace may be due to the lithology and the long-term cumulative displacement along the fault. In the Sencca sector, the fault scarps displace fluvio-glacial deposits whereas in the Pumamarca sector the fault scarps displace Paleogene-Neogene basement rocks and Quaternary alluvial deposits. The Paleogene-Neogene rocks outcropping in the Pumamarca sector are composed of poorly lithified siltstones and sandstones. The small values of the fault throw correspond to measurements made on outcrops of these loose siltstones, while the higher throw values correspond to measurements made on outcrops of more competent sandstones (Figure 3b).

The variability of the throw values may also reflect the variability of the cumulative displacement along the Pumamarca sector. The displacement is not representative of a single surface rupture event or a specific number of surface rupture events. This implies that coseismic ruptures can occur at various sites along the fault but are not necessarily confined to one single fault scarp. Finally, the variability of the cumulative displacement may be also linked to unrecognized fault geometry changes (e.g., dip angle) along the fault segment.

The Larapa sector corresponds to the eastern termination of the Tambomachay Fault (Figures 3 and 4a). The fault in this sector is mapped to run for ~5 km along the contact between the steep footwall topography and the south-dipping alluvial fan surfaces that drape off the fault footwall. Many of the fan surfaces have recently been covered by crop fields and houses, largely erasing the trace of any fault scarps (Figure 4a and 4b). Therefore, we were not able to measure any scarp offsets in the Larapa sector from the Pléiades DEM. However, we identified scarps along the contact between the footwall and the fan surfaces in the 1956 aerial photographs of the region that pre-date the urbanisation in the area. These scarps are short and run across sections of the range front between the ~N–S draining river valleys where they have avoided erosion. We interpret these scarps to suggest that this section of the Tambomachay Fault remains active, as it offsets the youngest fan surfaces in the region and may be active in future ruptures of the Tambomachay Fault.

3.3 Off-Fault Deformation in Alto Qosqo

In Alto Qosqo, located between the Pumamarca sector of the Tambomachay fault and Cusco, a series of previously unmapped, discontinuous scarps with a strike of $\pm$ 105°distributed in an area of 2 km^2 are visible in the 1956 aerial imagery (Figure 4c). Field investigation showed that these scarps are coincident with meter-offset normal faults with downthrow to the south clearly preserved in the near-surface stratigraphy, but the scarps have since been built upon (Figure 4c to 4f). The direction of motion and strike of these normal faults is consistent with the kinematics of the Cusco, Tambomachay, Qoricocha and Pachatusan Faults.

We interpret the Alto Qosqo scarps to be accommodating off-fault deformation within the region between the Cusco and Tambomachay Faults. Although these faults are small and therefore unlikely to generate significant earthquakes, they lie directly beneath the urbanised area of Alto Qosqo (Figure 4d). Therefore, even minor slip on these faults could cause differential ground motion beneath houses or across underground cables. Similar coseismic scarps have been observed previously within the footwall of the Parina normal fault that ruptured in a M$_w$ 6.1 earthquake 2016 (*Aguirre et al.*, 2021).

4 Dating of the Tambomachay Moraines and Determination of Holocene Slip Rate

4.1 Sample Preparation and Exposure Dating

In order to constrain the timing of the formation of the scarps along the Tambomachay Fault we focused on the Sencca sector, because the fault's morphology is well preserved in offset lateral moraines that have a relatively simple depositional history in this area (Figure 5a). To determine the age of the moraine surfaces, we sampled boulders along moraine crests located both above and below the fault scarps at Sennca Hill (Figure 5a and 5b). We extracted twelve samples in total, distributed along two major moraine crests (Figure 5a, 5b and Table SI-2, in the Supporting Information). The moraines were produced by accumulation of debris and boulders eroded from glacier cirques located a few hundred meters north (Figure 5c). Those glacier cirques were carved into quartz-rich red Paleogene sandstones showing almost vertical bedding planes. We collected the outermost 5 cm of rock from the top of the largest possible boulders, however we note the sampled boulders were relatively small (ranging between 0.5 to 1 m) compared to boulders routinely sampled for surface exposure dating (*Heyman et al.*, 2016). Because of their small sizes, post-glacial cover of the boulders may have occurred and may have variably shielded the boulders. To test for age consistency and uncertainty in our exposure age estimates, we sampled two replicates on two boulders closely located along one of the moraine crests (samples T10A and T10B). Those replicates returned the same exposure age within internal uncertainties (see below) thus providing evidence that that no post-glacial shielding had occurred.

Samples were prepared at the ISTerre GeoThermoChronology platform (Grenoble, France) following the chemical procedure of *Thorson Brown et al.* (1991) and *Merchel and Herpers* (1999). Rock samples were crushed, sieved (100–500 μm) and magnetic separation was performed using a Frantz©magnetic separator. The non-magnetic fraction was leached with a HCl-H$_2$SiF$_6$ mixture (1/3-2/3 vol.) to derive pure quartz. The ^{10}Be atmospheric compound was removed after three subsequent HF leachings (c. 10% dissolution each). After addition of ~150 ml of a concentrated carrier solution of ^{9}Be (3.025 $\pm$ 0.009x10-3 g ^{9}Be/g; *Merchel et al.*, 2008), the samples were completely dissolved in 40% HF. Beryllium was isolated by ion-exchange chromatography followed by selective pH precipitation techniques. The Be-hydroxides were precipitated, dried, and calcined at 850°C to produce BeO. ^{10}Be/^{9}Be ratio measurements were carried out at the French National AMS facility ASTER (*Arnold et al.*, 2010, 2013) located at the CEREGE laboratory (Aix-en-Provence) and calibrated
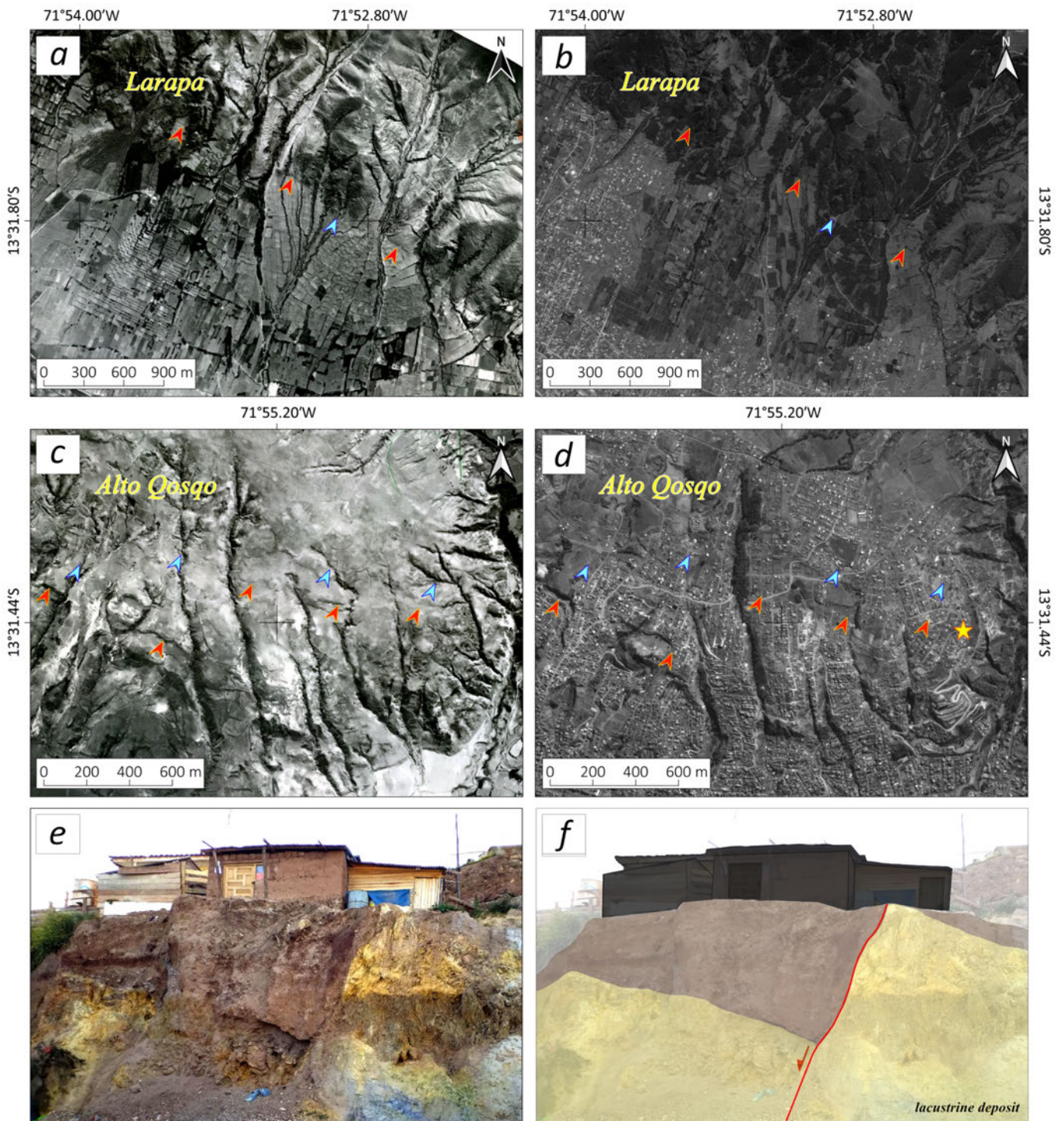
Figure 4 – Aerial photographs from 1956 and Pléiades satellite imagery from 2019 of the Tambomachay Fault. **a)** Orthomosaic constructed using images from 1956 showing that the most recent fault scarps (red marks) offset alluvial fans that drape off the range front in the Larapa sector. **b)** Orthomosaic constructed using images from 2019 showing the fault scarps (red marks) eroded by urban expansion and agricultural activity. **c)** The 1956 orthomosaic, shows the fault scarps pointed by the red marks and the streams by the blue marks, while **d)** the 2019 Orthomosaic shows how the Alto Qosqo sector of Cusco has covered the scarps in (c) and many of the streams have been infilled for construction. **e)** Field photograph located in the yellow star of the (d). **f)** House built on a small normal fault in the Alto Qosqo sector. In this sector the fault displaces Pleistocene lacustrine deposits.

against the "in-house standard" with an assumed 10Be/9Be ratio of 1.191 ± 0.013x10⁻¹¹ (*Braucher et al.*, 2015). Analytical uncertainties include the counting statistics, the machine stability (~0.5%; *Arnold et al.*, 2010) and the blank correction whose ¹⁰Be/⁹Be value was 1.58 ± 0.60x10⁻¹⁵ during the concerned measurement run (see Table SI-2, in the Supporting Information).

Exposure ages were computed from the 10Be measurements using the CREp program (*Martin et al.*, 2017). We applied the Lal-Stone scaling model with the ERA40 atmosphere model. Time-dependent
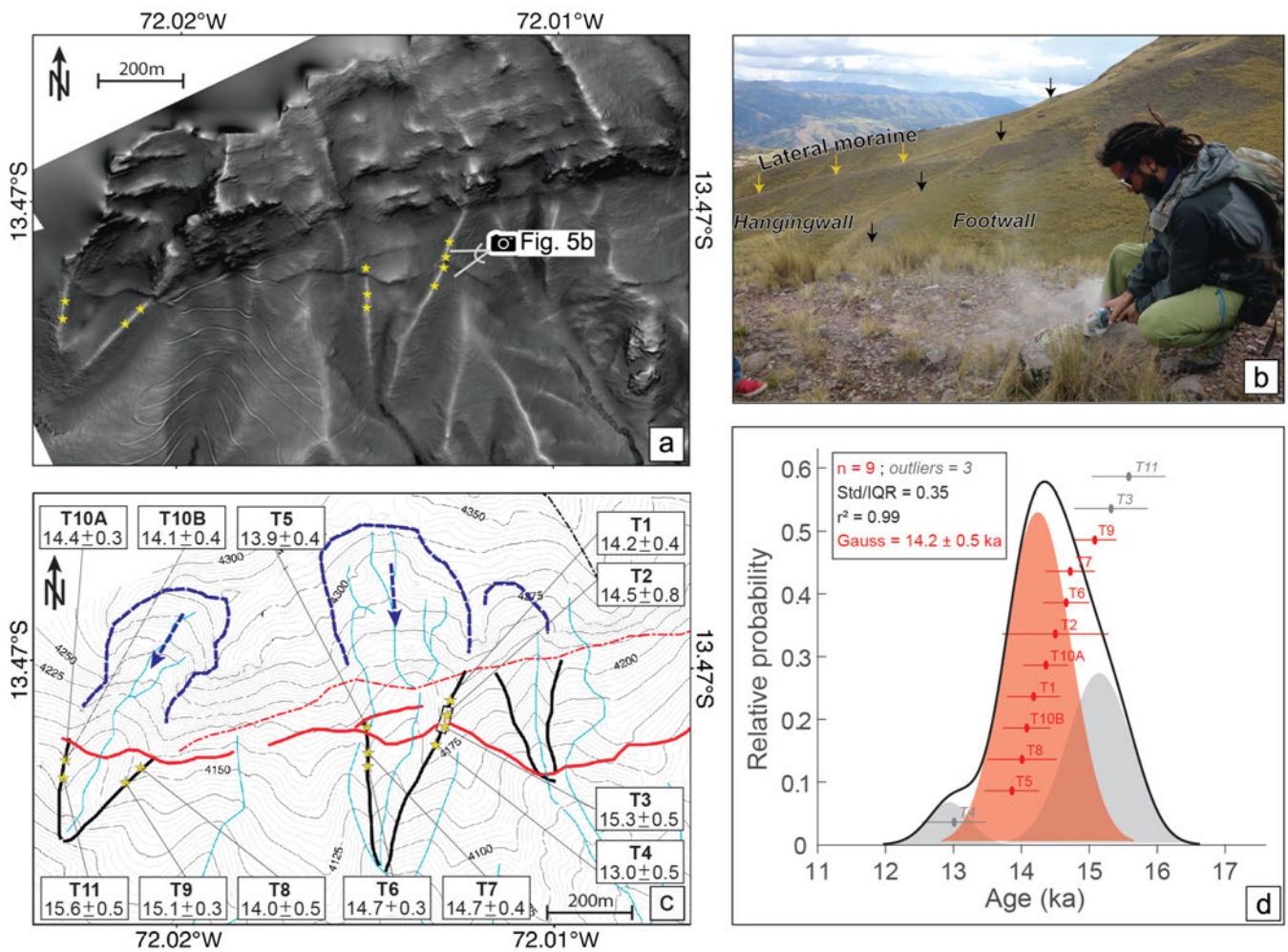
Figure 5 – **a)** Lateral moraines offset by the Tambomachay Fault (black line on the surface). Stars indicate the location of samples for cosmogenic dating. **b)** Field photograph of a lateral moraine offset by Tambomachay Fault and the moraine boulders sampling technique (location in a). **c)** Map with the same frame as Figure 5a showing the results of cosmogenic dating on lateral moraines (black lines) offset by active faults (red lines). The green rectangle indicates the location of the paleoseismic trench. Dashed blue lines indicate the top of the glacial cirques above the moraines and the dashed arrows indicate interpreted glacier flow direction. **d)** Probability density plot and statistics on the ages of the lateral moraines as analysed using the P-CAAT (*Dortch et al.*, 2022). The black line corresponds to the cumulative probability density estimate. The red shaded distribution is the highest probability component Gaussian with its corresponding ages reported in red text. Gray shaded distributions correspond to lower probability Gaussians related to outlier ages (in italic gray text) as detected by the P-CAAT tools for this dataset. Please refer to Figures SI-3 and SI-4, in the Supporting Information, to see individual analyses for each moraine that return a similar result.

corrections were performed using the *Muscheler et al.* (2005) geomagnetic database. Exposure ages were computed using a regionally averaged 10Be production rate value in quartz for the High Tropical Andes (weighted-mean of production rates from *Kelly et al.*, 2015; *Martin et al.*, 2015) that equals to 4.22 ± 0.13 at.g^{-1}.yr^{-1} (*Martin et al.*, 2017). Using a regionally averaged production rate has the advantage to be statistically more robust than single local calibration sites, accounting for possibly unrecognized geologic/geomorphic effects (e.g. erosion, partial shielding, inaccurate dating) associated with particular calibration sites. Moreover, it can overcome the relative inability of scaling schemes to account for regional peculiarities, for instance, due to atmospheric or geomagnetic anomalies that could not be adequately modelled in certain regions such as the High Central Andes

(*Martin et al.*, 2017). Because the sampled boulders did not show any trace of significant erosion, we computed the exposure ages assuming a denudation rate of zero. The assumption of zero denudation has been used by similar studies in the Peruvian Andes for periods covering the Late Pleistocene (e.g., *Bromley et al.*, 2009; *Martin et al.*, 2020). Exposure ages reported here should therefore be considered as minimum ages. Considering a denudation rate of 5x10^{-4} cm.yr^{-1} (value estimated by *Kelly et al.*, 2015) produces exposure age differences that are less than 5%, which remains within the analytical uncertainties (see Table SI-3, in the Supporting Information).

4.2 Exposure Dating Results

The ^{10}Be results and derived exposure ages are reported in Table SI-2 (in the Supporting Information).

Analytical uncertainties of $^{10}Be/^{9}Be$ measurements are low, ranging from 3–6%. Ratios of signals over blank are lower or equal to ± 3% which means that the blank correction does not affect the results as it falls below the analytical uncertainties. Derived exposure-ages range from 13.0 ± 0.5 to 15.6 ± 0.5 kyr (1σ). The two replicated samples, T10A and T10B, provide the same age, 14.4 ± 0.3 kyr and 14.1 ± 0.4 kyr respectively, both agreeing within uncertainties. For exposure age interpretation, we used the new Probabilistic Cosmogenic Age Analysis Tool (P-CAAT) by (*Dortch et al.*, 2022). Incorporating both sample age and geologic uncertainties, this tool that was specifically developed to estimation moraine landform age uses Monte Carlo simulations to eliminate dataset skewness by isolating component normal distributions from a cumulative probability density estimate. It allows outlier detection and provides the highest probability peak age for exposure age datasets (*Dortch et al.*, 2022). We first applied this tool on the eastern and western moraines separately (see Figures SI-3 and SI-4, in the Supporting Information). The highest-probability Gaussians give peaks at 14.51 ± 0.58 kyr (1 outlier) and 14.15 ± 0.47 kyr (2 outliers) for the eastern and the western moraines, respectively. As the values are indistinguishable within their uncertainties, this indicates that the two moraines edifices have the same age, which is consistent with the facts that they are close to each other in space (700 m) and that they both derive from similar glacial cirque areas at same elevation (Figure 5c). Processing the whole dataset with P-CAAT gives a similar result, with the same three outliers are detected (T3, T4 and T11) and a Gaussian distribution peak at 14.2 ± 0.5 kyr (Figure 5d). The distribution of exposure ages is thus well clustered (Figure 5d), which supports the view that unaccounted-for sources of uncertainty (such as differential denudation between boulders, partial shielding, surface lowering since the glacier retreat), if any, would be very low (<5%) and thus negligible. Calculating the exposure ages considering a denudation rate of 5×10^{-4} cm.yr^{-1} (see Table SI-3, in the Supporting Information), as quantified by *Kelly et al.* (2015) at a site located ~150 km southeast of Cusco, lead to a peak age of 14.9 ± 0.5 kyr, which remains with the uncertainty range of ages computed without denudation. The proposed timing of the moraine crest formation is well in line with several other glacial sediment records documented along the Altiplano (*Martin et al.*, 2020, and references therein), as well as that from the volcanos of the Western Cordillera (e.g., *Alcalá-Reygosa et al.*, 2017), which show major glacier advances and highstands of giant paleolakes on the Altiplano during the Heinrich Stadial 1a (i.e., 16.5–14.5 kyr BP; *Martin et al.*, 2018).

4.3 Holocene Fault Slip Rate at Sennca Hill

Given that the average amount of fault throw required to form the fault scarps offsetting the lateral moraines in the Sennca Hills is 4.0 ± 0.3 m, the dip angle of the fault plane in the paleoseismic trench is ranged from 50 to 70°and the moraines were formed 14.2 ± 0.5 kyr, the fault slip rate averaged over the Holocene is 0.30 to 0.37 mm/yr. This estimate is thought to be an upper bound, as we did not account for the effects of weathering on boulder surfaces for the exposure ages. One previous estimate of the slip rate (0.1–0.3 mm/yr; *Wimpenny et al.*, 2020) in the Alto Qosqo sector (Figure 3a) is slightly lower than our estimate, but our high-resolution DEMs yield a higher estimate of fault slip and we have tighter constraints on the timing of moraine formation from cosmogenic exposure dating than the ~8–45 kyr age used by *Wimpenny et al.* (2020). In the following section, we provide more details on the paleoseismic trenching to establish the timing of earthquakes on the Tambomachay Fault.
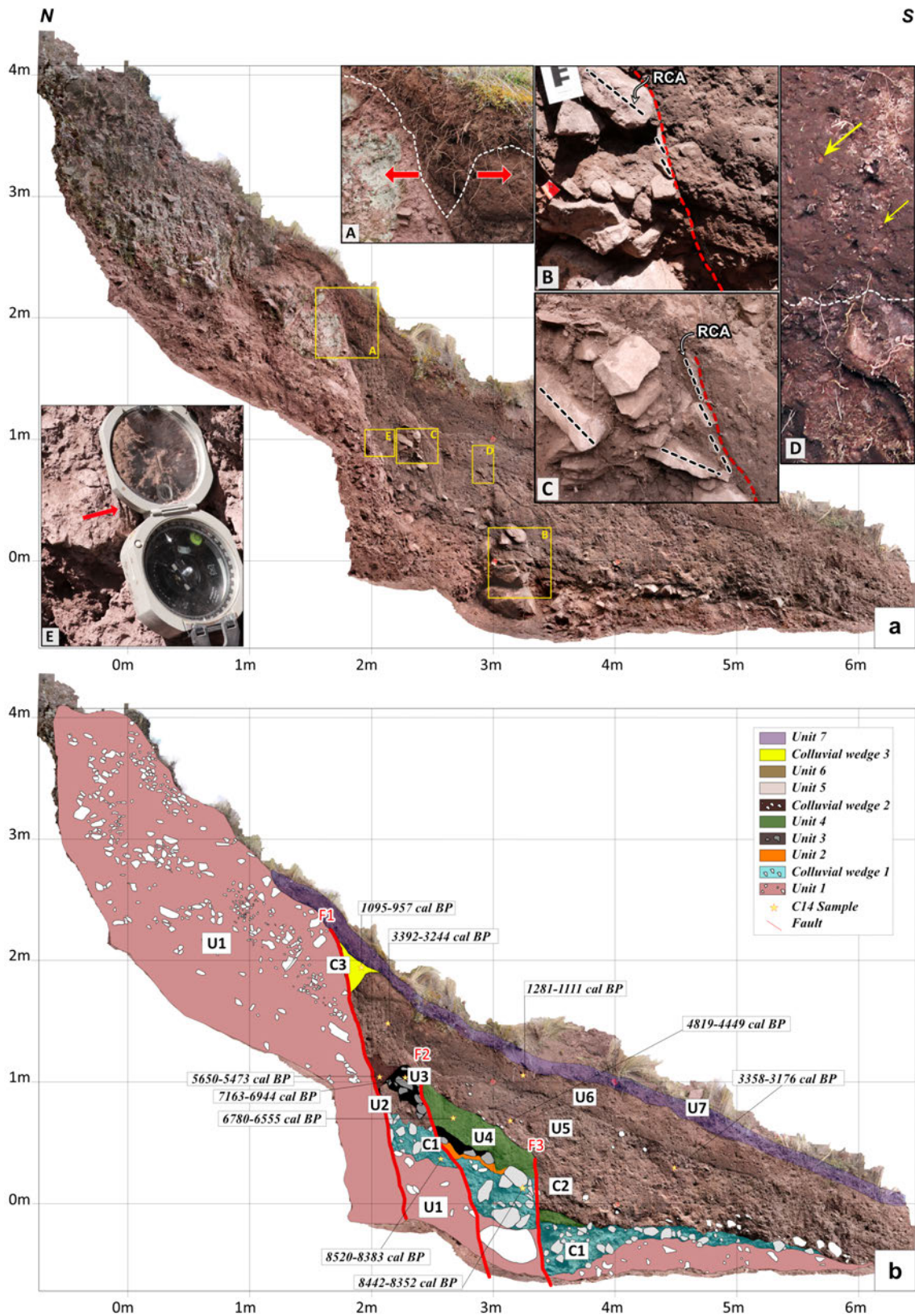
5 Paleoseismic Trenching

To determine a more detailed chronology of scarp formation, we opened a 7-m-long, 2-m-wide and 3-m-deep, N18°E-trending paleoseismic trench (S 13° 28′ 23.31″, W 72° 00′ 36.97″) across the fault scarp at Sennca Hills (Figure 5c). We selected this sector because the preserved morphology of the fault scarps allowed good estimation of the accumulated displacement since the Last Glacial Maximum (~14 kyr) (Figures 3 and 5).

We followed the standard cleaning, recording and analysis protocol proposed by *McCalpin* (2009). We collected organic sediment samples from the displaced layers and the colluvial wedges for radiocarbon dating. Each sample was placed in a foil packet and dated by the accredited Beta Analytic Laboratory in Miami. We used all the radiocarbon ages to build an OxCal stratigraphic model to estimate the most probable timing of the scarp-forming event(s), which were identified from offsets in the stratigraphy (*Ramsey*, 2017, 2018). The calibrations for the radiocarbon age of each sample were computed using the SHCal20 calibration curve (*Hogg et al.*, 2020).

5.1 Trench Stratigraphy and Radiocarbon Dating

A photomosaic and an interpreted log of the trench stratigraphy (east wall) demonstrating the lithological units defined by grain size, sorting, composition, color and sedimentary structures are shown in Figure 6a and 6b.

Figure 6 – Paleoseismic trench crossing the Tambomachay Fault in the Sencca sector. **a)** Photomosaic of east wall of the trench, exposing the Tambomachay Fault and evidence for earthquake surface ruptures. The yellow rectangles represent the location of close-up photographs of the trench wall shown in A, B, C, D and E. **A)** Tension crack delimited by the white dashed lines, associated with the most recent surface rupture of the Tambomachay Fault **B)** Clast rotation subparallel to the fault plane (red line) with the clast axes are represented by black dashed lines (RCA=Rotated Clast Axis). **C)** Clast rotation and the development of an imbricate fabric subparallel to the fault plane where the clast axes are represented by the white dashed lines. **D)** Lithological and texture differences between the U5 and C2. The yellow arrows point to red soft clasts in U5. The white dashed line is the contact between U5 and C2. **E)** The red arrow points to the slickenlines on the fault plane. **b)** Log of Holocene deposits deformed by Tambomachay Fault. The full description of each unit is given in the main text. See Figure SI-6, in the Supporting Information, for the raw high resolution photomosaic of the trench.

5.1.1 General Stratigraphy

A planar, south-dipping surface 2 m from the northern end of the trench contains dip-slip slickenlines and directly corresponds with the surface scarp, suggesting it is the main normal fault plane (red line F1 in the trench log). The footwall is composed entirely of a clast-supported deposit of angular to sub-rounded pebbles and cobbles (Paleogene sandstone) with a sandy, reddish silt matrix that we interpret to be the moraine deposits formed ~13-14 kyr (unit 1) (Figure 6a and 6b). The base of the hanging-wall of the trench is formed by the moraine deposits (unit 1) but is overlain by finer-grained colluvial deposits, that are in contact with the main fault F1, which in turn are displaced by the secondary faults F2 and F3. The fault plane F2 and F3 are sub-parallel to the main fault plane F1. The total thickness of sediment across the exposed section in the hanging-wall is ~2 m, while ~4 m vertical offset was recorded by the moraine surface measured from the high-resolution DEMs (Figure 3c).

5.1.2 Hanging-wall Stratigraphy

The stratigraphy in the hanging-wall consists of a succession of offset wedges of sediment that have distinctive stratigraphic features, which we describe below from the base (oldest) to the top (youngest). One common characteristic is the lithology of the clasts, which are all coming from the moraine and correspond to the red Paleogene sandstones.

At the base of the trench right next to the fault surface (F1), we have identified a ~50-cm-thick matrix-supported unit (U1) with a reddish-brown color. U1 is laterally discontinuous and appears to be displaced by faults F2 and F3. U1 is quite compact, composed of silt and sand, and exhibits moderate sorting. The clasts account for about 30% of the total deposit volume. They vary in shape from angular to subrounded, with an average diameter of 5 cm, and the largest clast measures 43 cm in diameter. This unit is interpreted to have formed in a glacial environment and corresponds to the moraine deposit of approximately 14 000 years ago (Figure 5), which is more prominently exposed at the base of the footwall.

On top of U1, there is a clast-supported deposit (C1) that varies laterally in thickness. The thickness adjacent to fault F1 is ~31 cm, while it is ~8 cm towards the southern end of the trench, forming a wedge shape. C1 has a dark brown color, is characterized by poorly sorted clasts and composed of compact material. The matrix is composed of silt and sand. The clasts represent 65% of the total deposit volume. Their shape varies from subrounded to subangular, with an average diameter of 9 cm, and the largest clast measures 24 cm in diameter. Clasts in contact with the F1 and F3 faults exhibit a rotated clast fabric, with their axis being subvertical and subparallel to the faults. The sediments in this deposit are colluvial and similar to those of U1, suggesting that they

originate from the footwall. Radiocarbon dating was performed on two samples collected from the base and center of C1, yielding ages of 8.5–8.4 kyr cal BP and 8.4–8.3 kyr cal BP, respectively. These ages are identical considering their uncertainties and suggest that at least 5-6 thousand years have passed between the emplacement of the lateral moraines (ca. 14 kyr ago) and the formation of C1 (at approximately 8.4 kyr cal BP).

The contact between C1 and the overlying sediment units (U2, U4, and C2) exhibits several discontinuities and appears to be displaced by faults F2 and F3 (Figures 6a and 6b).

In the central part of the trench, between F1 and F3, we found a fine-grained deposit of dark brown color (U2) overlying C1. U2 has a laterally variable thickness, being about 20 cm near F1 and decreasing to ~8 cm between F2 and F3. This deposit is interpreted as a wash facies originating from the footwall.

In erosive contact with U2, we found a dark brown, clast-supported deposit labeled U3. The unit U3 has an irregular and discontinuous shape, and its thickness also varies laterally, ranging from ~30 cm to ~10 cm between F1 and F2 and between F2 and F3, respectively. The base of U3 appears to have been displaced by the F2 fault. U3 is poorly sorted, and its matrix is primarily composed of sand and silt. The clasts represent about 70% of its total volume. The clasts have shapes ranging from angular to subrounded, with an average diameter of 8 cm, and the longest clast has a diameter of 15 cm. Clasts in contact with the F2 fault exhibit a rotated clast fabric, where the clast axes are subparallel to the fault. The sediments are similar to those in deposits C1 and U1, and they originate from the footwall. It is worth noting that the top of U3 to the north of the F2 fault is erosive. A radiocarbon analysis of organic sediment from U3 indicates an age of 7.2–6.9 kyr cal BP. To the south of the F2 fault and directly overlying U3, we observed a fine-grained deposit that is dark brown in color. It consists primarily of silts, clays, and sands. It exhibits lateral discontinuity due to displacement by the fault F3. The thickness of the deposit varies, being ~23 cm between F2 and F3 and getting thinner to ~9 cm to the south of F3, forming a wedge shape. Radiocarbon dating of U4 indicates an age of 6.8-6.6 kyr cal BP.

In erosive contact with U3, U4, and C1, we found a poorly sorted, light-brown-colored matrix-supported deposit called C2. C2 has a laterally varying thickness along the trench. Adjacent to the fault plane F1, the base of the deposit exhibits an inverted triangle shape with a thickness of 50 cm. South of fault F2 its thickness is 10 cm, covering the fault F2. However, adjacent to fault F3, its thickness increases to 70 cm, decreasing towards the southern termination of the trench in a wedge shape. The clasts represent 10% of the deposit volume. They are primarily exposed at the base of the deposit south of faults F2 and F3.

The clasts exhibit varying shapes from subangular to subrounded. The average clast diameter is 4 cm, with the largest clast measuring 9 cm in diameter. The orientation of the clasts in the U4 layer between faults F2 and F3, is parallel to the surface of U4. However, south of fault F3 the clasts are arranged chaotically without a preferred orientation. Two organic sediment samples were dated near fault plane F1 at the base of the deposit and near the top of deposit C2, providing ages of 5.7–5.5 kyr cal BP and 4.8–4.5 kyr cal BP, respectively.

In addition, we have identified a moderately sorted, light brown matrix supported deposit (U5) that is in erosive contact with layer C2. U5 has a constant thickness of ~32 cm. The clasts represent about 35% of the total volume. These clasts have a subangular shape with an average diameter of 1.5 cm and the largest clast measures ~6 cm in diameter. Additionally, a distinctive feature of this deposit is the presence of soft, millimeter-sized clasts with an orange color. It is important to note that a significant number of roots are observed towards the top of this unit. Two samples were extracted from U5 for radiocarbon dating, yielding roughly the same age interval of 3.4–3.2 kyr cal BP. While the faults F2 and F3 cut through the underlying units, they interestingly do not intersect U5, indicating that F2 and F3 predate U5 and that they were not active since ca. 3.4–3.2 kyr cal BP.

On top of U5, we identified a fine-grained deposit with a dark brown color, labeled U6. The unit U6 has a consistent thickness of ~27 cm all along the hanging-wall. This deposit is mainly composed of clays, silts, and sands and yields an age of 1.3–1.1 kyr cal BP for a sample extracted near its top.

We have identified a final deposit (C3) located between fault plane F1 and U5, a dark brown matrix-supported deposit. The matrix mainly consists of fine-grained silts and sands. The shape of C3 is distinctive, resembling an inverted triangle. Near its base, we observed clasts with subvertical axes. The clasts occupy about 5% of the deposit volume. They exhibit an angular shape, with an average diameter size of 1.5 cm, and the largest clast has a diameter of 2 cm. It is noteworthy that a significant number of roots were found within this deposit.

The whole trench is sealed by the unit U7, a shallow (~10 cm) silty-clay layer including fresh roots and vegetation at surface.

5.2   Reconstruction of the Trench Stratigraphy

We reconstructed the trench stratigraphy to model the different stages of fault-related vertical deformation, deposition, and erosion. In this model, we account for the vertical component of the displacement and the thickness of geologic units present during each event and ignore the effects of sediment compaction. However, it is not possible to precisely reconstruct the amount of erosion and sedimentation that might have taken place at each stage of the geological history.

We calculate a minimum offset for each event from the current footwall morphology in the trench and the thicknesses of the colluvial wedges. We correlate the current top of the footwall with the tops of the displaced stratigraphic levels identified in the hanging-wall.

Timing constraints on the model are provided by the bulk radiocarbon dates of the different units (see Table SI-4, in the Supporting Information). Bulk radiocarbon dating of sediment samples, as opposed to dating individual pieces of plant or animal matter, can have age uncertainties significantly larger than the analytical uncertainties (~1 kyr compared to ~0.2 kyr), due to the inheritance of older material through bioturbation and reworking within bulk samples (e.g., *Grützner et al.*, 2016). One effect can be that bulk radiocarbon age of different units are not necessarily in stratigraphic order when taking into account the analytical uncertainties alone. However, within the Sencca Hills trench, we find that all the radiocarbon ages are in stratigraphic order within their analytical uncertainties. Therefore, we assume that the bulk radiocarbon dates and their analytical uncertainties are representative of the true age uncertainties (Figure 7) and are good estimates of the layer ages (*Ramsey*, 2018).

Event 1 is characterized by slip on the fault F1 and is the first event to offset the moraine deposits (unit 1). Erosion of the resulting fault scarp formed the colluvial wedge 1 (C1) with a thickness of about 0.4 m which gives a rough estimate of the displacement for this event. Given the age of the colluvial wedge 1 and the underlying moraines, the first event occurred between 13–14 kyr and 8.5–8.3 kyr.

Event 2 occurred after the deposition of unit 4 and is characterized by slip on the main fault F1 and the two smaller faults F2 and F3. Erosion of the resulting escarpments forms the colluvial wedge C2 and the accommodation space for the deposition of units 5 and 6. The minimum displacement for this event is 1.4 m. This event occurred between 6.8–6.6 kyr and 5.7–5.5 kyr.

Event 3 is characterized by the reactivation of fault F1, with the formation of a tensional crack adjacent to the fault plane and the erosion of the new scarp forming a third colluvial wedge (C3). Event 3 occurred between 1.2–1.1 kyr and 1.1–1.0 kyr, had a minimum offset of ~0.35 m, and pre-dated all of the earthquakes within the historical record.

The accumulated thickness of sediments in the trench is ~2 m, in comparison with the vertical offset of the fault (3.5 m) calculated from the perpendicular profile on the moraine. Thus, there is a vertical
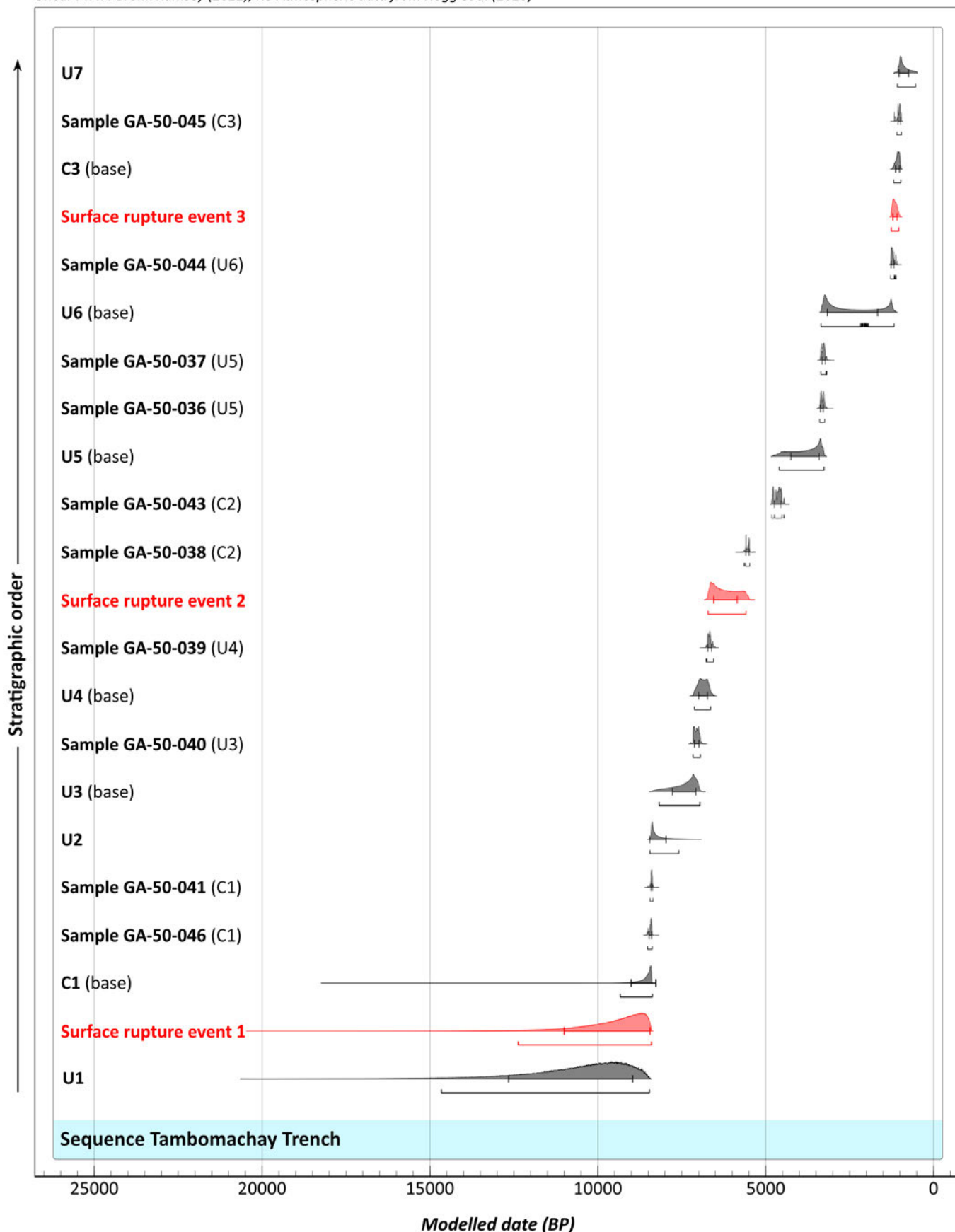
Figure 7 – OxCal Bayesian statistical age model of calibrated ^{14}C ages for the trench with resulting modeled age ranges for Holocene earthquakes. Stratigraphic units are reported from the oldest to the youngest, from bottom to top, respectively. Probability density functions for each sample give the range of ages possible for each surface rupture event (see *Ramsey*, 2017).

offset of ~1.5 m of the fault that is not compensated by sedimentation in the trench. Considering the minimum value of the most recent event in the trench (~0.35 m), there is 3.15 m of geomorphic offset across the fault scarp possibly accumulated between the first and the second event. We estimate that each event could be associated with ~1.5 m of slip.

5.3 Paleomagnitudes of Earthquakes on the Tambomachay Fault

An upper bound on the paleomagnitude of the past earthquakes on the Tambomachay Fault can be estimated from the surface fault slip (u), the fault length (L) and an estimate of the down-dip width of the fault (W) using the expression: $M = cuLW$ (Kanamory and Anderson, 1975; Hanks, and Kanamori, 1979), where c is the shear modulus of the crust. The fault length is constrained to be ~20 km from the length of fault scarps mapped using the high-resolution DEMs and optical satellite imagery and the geomorphological expression of the fault. The down-dip width of the seismogenic portion of the fault can be computed from the range of average normal fault dips (45°– 60°) (*Jackson and White*, 1989) and the thickness of the seismogenic layer in the Andes determined from body-waveform modelling past earthquakes (10–15 km; *Wimpenny et al.*, 2018). The fault throws from our paleoseismic trench vary between 0.4–1.4 m, which is equivalent to 0.5–2 m of slip during one seismic event on a 45°–60° dipping fault with a pure dip-slip slip vector. Using a shear modulus of 30 GPa, the range of paleomagnitudes of the earthquakes preserved in the Tambomachay trench could be up to M_w 6.4–6.9. Empirical relations between earthquake magnitude and fault characteristics suggest similar ranges of paleomagnitudes such as: (1) ~6.2 M_w solely based on the 20-km fault length (*Thingbaijam et al.*, 2017), which would be a minimum M_w bound in the case of the Tambomachay fault; (2) M_w 6.5–6.9 taking into account the fault slip measured in the trench (0.5–2 m), assuming that theses displacements are representative for the 20-km fault length and applying the *Wells and Coppersmith* (1994) equations; and (3) M_w 6.7 to 7.6 with the same configuration as previously mentioned but applying the *Thingbaijam et al.* (2017) equation.

6 Discussion

The trenching and geomorphological analysis have shown that at least three surface-rupturing earthquakes with metrer-scale surface offsets occurred on the Tambomachay Fault at Sennca Hills between 13–14 kyr and ~1 kyr. These earthquakes pre-date those in 1400–1500 CE, 1650 CE, and 1950 CE mentioned in the historical record of earthquake shaking in Cusco city. Therefore, the earthquakes in the historical record were most likely generated by ruptures on another fault in the region or they did not rupture the surface of the Tambomachay

Fault. The Pachatusan or Cusco faults are the most likely alternatives, as they are clearly expressed in the geomorphology of the basin and have no paleoseismic trenching results to rule them out, but other un-mapped faults may also have been responsible.

Our new constraints on the age of the moraines cut by the Tambomachay Fault allow for a more accurate estimate of the fault's Holocene-average slip rate (ranged from 0.30 to 0.37 mm/yr) than presented in previous studies (e.g., *Wimpenny et al.*, 2020). The new fault slip rate is equivalent to ~30 cm of slip deficit accumulating every thousand years. Under the assumption that this slip rate represents the time-averaged rate over the Quaternary, the 300 m-high ridge line marked by triangular facets that run around the northern margin of the Cusco Basin could have been formed within less than 1 Myrs, placing a tentative rough bound on the age of the extensional faulting around Cusco. However, the accumulated displacement might be larger as part of the fault plane is beneath the sedimentary cover of the Cusco Basin and some erosion would be expected on longer time scales. Thus, the estimation of the initiation of the extensional faulting should be considered as a lower bound only.

Given that the last recorded earthquake in the Sennca Hills trench was ~1 kyr, at least a 30 cm slip deficit may have accumulated on the Tambomachay Fault since it last ruptured the surface.

The new earthquake history on the Tambomachay Fault from our trenching also provides important insight into the seismic hazard in the Cusco Basin. The largest earthquake recorded by seismometers in the region was the M_w 5.3 1986 earthquake near Qoricocha, which generated minor cracks at the surface and had a hypocenter located north of the basin. The shaking intensities within the basin reached V–VI on the modified Mercalli scale (*Cabrera and Sébrier*, 1998). The damage distribution in the larger magnitude 1950 earthquake was also well recorded. Intensities of VII on the modified Mercalli scale were observed within the Cusco Basin. Sparse seismological recordings estimated the magnitude of the 1950 earthquake as M ~6, which is similar to the estimated magnitude of the surface-rupturing earthquakes recorded in the trench at Sencca Hills. Therefore, future ruptures on the Tambomachay Fault have the potential to generate seismic shaking at intensities of at least VII throughout the Cusco Basin. Given the recent expansion of the city onto the steep slopes surrounding the basin's margins, particularly around Sennca Hills, the exposure to seismic shaking has also significantly increased since the last major earthquake in the region.

7 Conclusions

We identified and mapped 20 km of fault scarps along the Tambomachay Fault north of the city of Cusco,

Peru. At the western end of the fault at Sencca Hill, ca. 4 ± 1 m-high fault scarps cut lateral moraines dated to have formed at 14.2 ± 0.5 kyr based on 10Be cosmogenic-exposure dating of glacial boulders on the moraine crests. When combined with knowledge of the fault geometry, the scarp offset and moraine age yield a Holocene slip rate on the Tambomachay Fault of 0.30 to 0.37 mm/yr. Paleoseismic trenching revealed a series of offset colluvial wedges within the hanging wall of the moraine crest scarps at Sencca Hill, which we interpreted to reflect three surface-rupturing earthquakes on the Tambomachay Fault in the last 8–9 kyr. Radiocarbon dating and reconstruction of the trench stratigraphy identified three earthquakes with offsets between 0.4 m and 1.4 m. The identified Tambomachay Fault ruptures predate Inca times (>1 kyr), so we suggest that the earthquakes that affected the Incas occurred on other fault strands adjacent to the city of Cusco or that they did not rupture the surface. Using estimates of the length and down-dip width of the fault, the magnitude of these earthquakes would have been M_w 6.4–6.9 — far higher than any earthquakes in the Cusco Basin that have occurred since the advent of modern seismology. An earthquake of M_w 6 close to the 500 000 inhabitants of Cusco city has the capacity to cause wide-spread damage, particularly given the recent development on the steep slopes along the northern margins of the Cusco Basin.

Acknowledgements

Author contributions

Lorena Rosell: Designer of the study, fieldwork, interpretations, figures and writer. **Carlos Benavente**: Designer of the study, fieldwork, interpretations, figures and writer. **Swann Zerathe**: Fieldwork, interpretations, figures and writer. **Sam Wimpenny**: Interpretations, figures and writer. **Enoch Aguirre**: Fieldwork, interpretations, figures and DEM building. **Richard Walker**: Fieldwork, interpretations and writer. **Christoph Grützner**: Fieldwork, interpretations and writer. **Briant García**: Fieldwork, interpretations, DEM building and writer. **Laurence Audin**: Interpretations and writer. **Andy Combey**: Interpretations. **Anderson Palomino**: Interpretations and figures. **Fabrizio Delgado**: Interpretations and fieldwork. **Miguel Rodríguez-Pascua**: Interpretations and fieldwork. **José Cardenas**: Interpretations and fieldwork. **Julien Carcaillet**: Interpretations.

Data availability

The data underlying this article are available in the article and in the Supporting Information. The DEM data used in this work can be downloaded from https://doi.org/10.5281/zenodo.8147580.

Competing interests

The authors declare no competing interests.

Peer review

This publication was peer-reviewed by Maryline Le Beon and Marthe Lefevre. The full peer-review report can be found here: tektonika.online/index.php/home/article/view/27/40

Copyright notice

References

Agisoft (2018), Agisoft PhotoScan User Manual - Professional Edition, Version 1.4.

Aguirre, E., C. Benavente, L. Audin, S. Wimpenny, S. Baize, L. Rosell, F. Delgado, B. García, and A. Palomino (2021), Earthquake surface ruptures on the altiplano and geomorphological evidence of normal faulting in the December 2016 (Mw 6.1) Parina earthquake, Peru, *Journal of South American Earth Sciences*, *106*, 103,098, doi: 10.1016/j.jsames.2020.103098.

Alcalá-Reygosa, J., D. Palacios, and L. Vázquez-Selem (2017), A preliminary investigation of the timing of the local last glacial maximum and deglaciation on HualcaHualca volcano - Patapampa Altiplano (arid Central Andes, Peru), *Quaternary International: the Journal of the International Union for Quaternary Research*, *449*, 149–160, doi: 10.1016/j.quaint.2017.07.036.

Arnold, M., S. Merchel, D. L. Bourlès, R. Braucher, L. Benedetti, R. C. Finkel, G. Aumaître, A. Gottdang, and M. Klein (2010), The French accelerator mass spectrometry facility ASTER: Improved performance and developments, *Nuclear Instruments & Methods in Physics Research. Section B, Beam Interactions*

with Materials and Atoms, *268*(11), 1954–1959, doi: 10.1016/j.nimb.2010.02.107.

Arnold, M., G. Aumaître, D. L. Bourlès, K. Keddadouche, R. Braucher, R. C. Finkel, E. Nottoli, L. Benedetti, and S. Merchel (2013), The French accelerator mass spectrometry facility ASTER after 4years: Status and recent developments on 36Cl and 129I, *Nuclear Instruments & Methods in Physics Research. Section B, Beam Interactions with Materials and Atoms*, *294*, 24–28, doi: 10.1016/j.nimb.2012.01.049.

Audin, L., C. David, S. Hall, D. Farber, and G. Hérail (2007), Geomorphic Evidences Of Recent Tectonic Activity In The Forearc, *Revista de la Asociacion Geologica Argentina*, *61*.

Benavente, C., F. Delgado, E. Taipe, L. Audin, and W. Pari (2013), Neotectónica y peligro sísmico en la región Cusco, *Tech. Rep. 55*, Instituto Geológico, Minero y Metalúrgico - INGEMMET, Lima.

Benavente, C., S. Zerathe, L. Audin, S. R. Hall, X. Robert, F. Delgado, J. Carcaillet, and ASTER Team (2017), Active transpressional tectonics in the andean forearc of southern peru quantified by 10Be surface exposure dating of an active fault scarp, *Tectonics*, *36*(9), 1662–1678, doi: 10.1002/2017tc004523.

Benavente, C., S. Wimpenny, L. Rosell, X. Robert, A. Palomino, L. Audin, E. Aguirre, and B. García (2021), Paleoseismic evidence of an M w 7 pre-Hispanic earthquake in the Peruvian forearc, *Tectonics*, *40*(6), doi: 10.1029/2020tc006479.

Benavente, C., A. Palomino, S. Wimpenny, B. García, L. Rosell, E. Aguirre, J. Macharé, A. M. Rodriguez Padilla, and S. R. Hall (2022), Paleoseismic evidence of the 1715 C.E earthquake on the Purgatorio Fault in Southern Peru: Implications for seismic hazard in subduction zones, *Tectonophysics*, *834*, 229,355, doi: 10.1016/j.tecto.2022.229355.

Beyer, R. A., O. Alexandrov, and S. McMichael (2018), The Ames stereo pipeline: NASA's open source software for deriving and processing terrain data, *Earth and space science (Hoboken, N.J.)*, *5*(9), 537–548, doi: 10.1029/2018ea000409.

Braucher, R., V. Guillou, D. L. Bourlès, M. Arnold, G. Aumaître, K. Keddadouche, and E. Nottoli (2015), Preparation of ASTER in-house 10Be/9Be standard solutions, *Nuclear Instruments & Methods in Physics Research. Section B, Beam Interactions with Materials and Atoms*, *361*, 335–340, doi: 10.1016/j.nimb.2015.06.012.

Bromley, G. R. M., J. M. Schaefer, G. Winckler, B. L. Hall, C. E. Todd, and K. M. Rademaker (2009), Relative timing of last glacial maximum and late-glacial events in the central tropical Andes, *Quaternary Science Reviews*, *28*(23), 2514–2526, doi: 10.1016/j.quascirev.2009.05.012.

Broxton, M. J., and L. J. Edwards (2008), The Ames Stereo Pipeline: Automated 3D Surface Reconstruction from Orbital Imagery, in *39th Lunar and Planetary Science Conference*, p. 2419, LPI Contribution.

Cabrera, J., and M. Sébrier (1998), Surface rupture associated with a 5.3-mb earthquake: The 5 April 1986 Cuzco earthquake and kinematics of the Chincheros-Quoricocha faults of the High Andes, Peru, *Bulletin of the Seismological Society of America*, *88*(1), 242–255, doi: 10.1785/BSSA0880010242.

Cabrera Nuñez, J. (1988), Néotectonique et sismotectonique dans la Cordillère andine au niveau du changement de géométrie de la subduction : la région

de Cuzco (Pérou), Ph.D. thesis, Paris 11.

Carlotto, V. (1998), Evolution andine et raccourcissement au niveau de Cusco (13°-16°S) , Pérou: Enregistrement sédimentaire, chronologie, contrôles paléogéographiques, évolution cinématique, Ph.D. thesis, Université Joseph-Fourier - Grenoble I.

Carlotto, V., J. Cardenas, and G. Carlier (2010), Mapa geológico del Cuadrángulo de Cusco, escala 1:50 000, Hoja 28-s, cuadrante-IV.

Clapperton, C. M. (1983), The glaciation of the Andes, *Quaternary Science Reviews*, *2*(2), 83–155, doi: 10.1016/0277-3791(83)90005-7.

Datos Sísmicos (2022), CENSIS - Instituto Geofísico Del Perú, https://ultimosismo.igp.gob.pe/datos-sismicos.

Dortch, J. M., M. D. Tomkins, S. Saha, M. K. Murari, L. M. Schoenbohm, and D. Curl (2022), A tool for the ages: The Probabilistic Cosmogenic Age Analysis Tool (P-CAAT), *Quaternary geochronology*, *71*, 101,323, doi: 10.1016/j.quageo.2022.101323.

Ekström, G., M. Nettles, and A. M. Dziewoński (2012), The global CMT project 2004–2010: Centroid-moment tensors for 13,017 earthquakes, *Physics of the Earth and Planetary Interiors*, *200-201*, 1–9, doi: 10.1016/j.pepi.2012.04.002.

Ericksen, G. E., J. F. Concha, and E. Silgado (1954), The Cusco, Peru, Earthquake of May 21, 1950, *Bulletin of the Seismological Society of America*, *44*(2A), 97–112, doi: 10.1785/BSSA04402A0097.

Gisbert, T. (1999), *El paraíso de los pájaros parlantes*.

Grützner, C., P. Fischer, and K. Reicherter (2016), Holocene surface ruptures of the Rurrand Fault, Germany—insights from palaeoseismology, remote sensing and shallow geophysics, *Geophysical Journal International*, *204*(3), 1662–1677, doi: 10.1093/gji/ggv558.

Heyman, J., P. J. Applegate, R. Blomdin, N. Gribenski, J. M. Harbor, and A. P. Stroeven (2016), Boulder height – exposure age relationships from a global glacial 10Be compilation, *Quaternary geochronology*, *34*, 1–11, doi: 10.1016/j.quageo.2016.03.002.

Hogg, A. G., T. J. Heaton, Q. Hua, J. G. Palmer, C. S. M. Turney, J. Southon, A. Bayliss, P. G. Blackwell, G. Boswijk, C. B. Ramsey, C. Pearson, F. Petchey, P. Reimer, R. Reimer, and L. Wacker (2020), SHCal20 Southern Hemisphere Calibration, 0–55,000 Years cal BP, *Radiocarbon*, *62*(4), 759–778, doi: 10.1017/RDC.2020.59.

Huamán, R. (1987), Aspectos sismotectónicos del sismo del Cuzco del 5 de abril de 1986, *Tech. rep.*, IGP, Lima.

Jackson, J. A., and N. J. White (1989), Normal faulting in the upper continental crust: observations from regions of active extension, *Journal of Structural Geology*, *11*(1), 15–36, doi: 10.1016/0191-8141(89)90033-3.

Kelly, M. A., T. V. Lowell, P. J. Applegate, F. M. Phillips, J. M. Schaefer, C. A. Smith, H. Kim, K. C. Leonard, and A. M. Hudson (2015), A locally calibrated, late glacial 10Be production rate from a low-latitude, high-altitude site in the Peruvian Andes, *Quaternary Geochronology*, *26*, 70–85, doi: 10.1016/j.quageo.2013.10.007.

Macharé Ordoñez, J., C. L. Benavente Escobar, and L. Audin (2009), Síntesis descriptiva del mapa neotectónico 2008 - [Boletín C 40], *Instituto Geológico, Minero y Metalúrgico - INGEMMET*.

Machette, M. N. (2000), Active, capable, and potentially active faults — a paleoseismic perspective,

Journal of Geodynamics, *29*(3), 387–392, doi: 10.1016/S0264-3707(99)00060-5.

Mackenzie, D., and A. Elliott (2017), Untangling tectonic slip from the potentially misleading effects of landform geometry, *Geosphere*, *13*(4), 1310–1328, doi: 10.1130/GES01386.1.

Martin, L. C. P., P.-H. Blard, J. Lavé, R. Braucher, M. Lupker, T. Condom, J. Charreau, V. Mariotti, ASTER Team, and E. Davy (2015), In situ cosmogenic 10Be production rate in the High Tropical Andes, *Quaternary Geochronology*, *30*, 54–68, doi: 10.1016/j.quageo.2015.06.012.

Martin, L. C. P., P.-H. Blard, G. Balco, J. Lavé, R. Delunel, N. Lifton, and V. Laurent (2017), The CREp program and the ICE-D production rate calibration database: A fully parameterizable and updated online tool to compute cosmic-ray exposure ages, *Quaternary Geochronology*, *38*, 25–49, doi: 10.1016/j.quageo.2016.11.006.

Martin, L. C. P., P.-H. Blard, J. Lavé, T. Condom, M. Prémaillon, V. Jomelli, D. Brunstein, M. Lupker, J. Charreau, V. Mariotti, B. Tibari, ASTER Team, and E. Davy (2018), Lake Tauca highstand (Heinrich Stadial 1a) driven by a southward shift of the Bolivian High, *Science Advances*, *4*(8), eaar2514, doi: 10.1126/sciadv.aar2514.

Martin, L. C. P., P.-H. Blard, J. Lavé, V. Jomelli, J. Charreau, T. Condom, M. Lupker, M. Arnold, G. Aumaître, D. L. Bourlès, and K. Keddadouche (2020), Antarctic-like temperature variations in the Tropical Andes recorded by glaciers and lakes during the last deglaciation, *Quaternary Science Reviews*, *247*, 106,542, doi: 10.1016/j.quascirev.2020.106542.

McCalpin, J. (2009), *Paleoseismology*, International geophysics series, 2nd ed ed., Academic Press, Burlington, MA.

McQuarrie, N., T. A. Ehlers, J. B. Barnes, and B. Meade (2008), Temporal variation in climate and tectonic coupling in the central Andes, *Geology*, *36*(12), 999–1002, doi: 10.1130/G25124A.1.

Merchel, S., and U. Herpers (1999), An Update on Radiochemical Separation Techniques for the Determination of Long-Lived Radionuclides via Accelerator Mass Spectrometry, *Radiochimica Acta*, *84*(4), 215–220, doi: 10.1524/ract.1999.84.4.215.

Merchel, S., M. Arnold, G. Aumaître, L. Benedetti, D. L. Bourlès, R. Braucher, V. Alfimov, S. P. H. T. Freeman, P. Steier, and A. Wallner (2008), Towards more precise 10Be and 36Cl data from measurements at the 10−14 level: Influence of sample preparation, *Nuclear Instruments & Methods in Physics Research. Section B, Beam Interactions with Materials and Atoms*, *266*(22), 4921–4926, doi: 10.1016/j.nimb.2008.07.031.

Mercier, J. L., M. Sebrier, A. Lavenu, J. Cabrera, O. Bellier, J.-F. Dumont, and J. Machrare (1992), Changes in the tectonic regime above a subduction zone of Andean Type: The Andes of Peru and Bolivia during the Pliocene-Pleistocene, *Journal of Geophysical Research*, *97*(B8), 11,945, doi: 10.1029/90jb02473.

Molnar, P. (1979), Earthquake recurrence intervals and plate tectonics, *Bulletin of the Seismological Society of America*, *69*(1), 115–133, doi: 10.1785/BSSA0690010115.

Muscheler, R., J. Beer, P. W. Kubik, and H.-A. Synal (2005), Geomagnetic field intensity during the last 60,000 years based on 10Be and 36Cl from the Summit ice cores and 14C, *Quaternary science reviews*, *24*(16), 1849–1860, doi: 10.1016/j.quascirev.2005.01.012.

Oncken, O., D. Hindle, J. Kley, K. Elger, P. Victor, and K. Schemmann (2006), Deformation of the Central Andean Upper Plate System — Facts, Fiction, and Constraints for Plateau Models, in *The Andes: Active Subduction Orogeny*, edited by O. Oncken, G. Chong, G. Franz, P. Giese, H.-J. Götze, V. A. Ramos, M. R. Strecker, and P. Wigger, Frontiers in Earth Sciences, pp. 3–27, Springer Berlin Heidelberg, Berlin, Heidelberg, doi: 10.1007/978-3-540-48684-8_1.

Palma, R. (1901), *Anales del Cuzco, 1600 á 1750*, "El Estado.

Ramsey, B. (2018), ORAU - OxCal Program, v.4.3: Radiocarbon Accelerator Unit.

Ramsey, C. B. (2017), Methods for Summarizing Radiocarbon Datasets, *Radiocarbon*, *59*(6), 1809–1833, doi: 10.1017/RDC.2017.108.

Sébrier, M., J. L. Mercier, F. Mégard, G. Laubacher, and others (1985), Quaternary normal and reverse faulting and the state of stress in the central Andes of south Peru, *Tectonics*, *4*(7), 739–780, doi: 10/dv7bkj.

Silgado, E. (1978), Historia de los sismos más notables ocurridos en el Perú (1513 -1974), *Tech. rep.*, Instituto de Geología y Minería.

Tavera, H., C. Agüero, and E. Fernández (2016), Catálogo general de isosistas para sismos peruanos, *Tech. rep.*, Instituto Geofísico del Perú, Lima.

Thingbaijam, K. K. S., P. Martin Mai, and K. Goda (2017), New empirical earthquake source-scaling laws, *Bulletin of the Seismological Society of America*, *107*(5), 2225–2246, doi: 10.1785/0120170017.

Thorson Brown, E., J. M. Edmond, G. M. Raisbeck, F. Yiou, M. D. Kurz, and E. J. Brook (1991), Examination of surface exposure ages of Antarctic moraines using in situ produced 10Be and 26Al, *Geochimica et Cosmochimica Acta*, *55*, 2269–2283, doi: 10.1016/0016-7037(91)90103-C.

Villegas-Lanza, J. C., M. Chlieh, O. Cavalié, H. Tavera, P. Baby, J. Chire-Chira, and J.-M. Nocquet (2016), Active tectonics of Peru: Heterogeneous interseismic coupling along the Nazca megathrust, rigid motion of the Peruvian Sliver, and Subandean shortening accommodation, *Journal of Geophysical Research, [Solid Earth]*, *121*(10), 7371–7394, doi: 10.1002/2016jb013080.

Wells, D. L., and K. J. Coppersmith (1994), New empirical relationships among magnitude, rupture length, rupture width, rupture area, and surface displacement, *Bulletin of the Seismological Society of America*, *84*(4), 974–1002, doi: 10.1785/BSSA0840040974.

Westoby, M. J., J. Brasington, N. F. Glasser, M. J. Hambrey, and J. M. Reynolds (2012), 'Structure-from-Motion' photogrammetry: A low-cost, effective tool for geoscience applications, *Geomorphology*, *179*, 300–314, doi: 10.1016/j.geomorph.2012.08.021.

Wimpenny, S., A. Copley, C. Benavente, and E. Aguirre (2018), Extension and Dynamics of the Andes Inferred From the 2016 Parina (Huarichancara) Earthquake, *Journal of Geophysical Research, [Solid Earth]*, *123*(9), 8198–8228, doi: 10.1029/2018JB015588.

Wimpenny, S., C. Benavente, A. Copley, B. Garcia, L. Rosell, A. O'Kane, and E. Aguirre (2020), Observations and dynamical implications of active normal faulting in South Peru, *Geophysical Journal International*, *222*(1), 27–53, doi: 10.1093/gji/ggaa144.